Talanta 108 (2013) 19–29

Contents lists available at SciVerse ScienceDirect

Talanta

journal homepage: www.elsevier.com/locate/talanta

Zeolite encapsulated Ni(II)-Schiff-base complex: A novel size-selective electro-catalyst for the determination of the purity of stevioside

Mehdi Rashvand avei [a], Majid Jafarian [a,*], Sedigheh Etezadi [a], Fereydoon Gobal [b], Maryam Khakali [a], Saeed Rayati [a], Mohammad Ghasem Mahjani [a]

[a] Department of Chemistry, K.N. Toosi University of Technology, P.O. Box 15875-4416, Tehran, Iran
[b] Department of Chemistry, Sharif University of Technology, P.O. Box 11365-9516, Tehran, Iran

ARTICLE INFO

Article history:
Received 4 October 2012
Received in revised form
20 February 2013
Accepted 21 February 2013
Available online 5 March 2013

Keywords:
NaY zeolite
Stevioside
Carbohydrates
Encapsulation
Modified electrodes
DFT
Schiff-base complexes

ABSTRACT

Ship-in-a-bottle complex of nickel(II) containing the ligand *N,N′*-bis(2,4-dihydroxyacetophenone)-2,2-dimethylpropandiimine (H_2{salnptn(4-OH)$_2$}) has been synthesized in zeolite Y. The characteristics of the encapsulated complex are identified by the methods of EDX, SEM, XRD, FT-IR and cyclic voltammetry. A catalytic effect in the electrochemical oxidation of glucose, fructose and sucrose, and a blocking effect in stevioside oxidation are demonstrated on the Ni^{II}{salnptn(4-OH)$_2$}-Y/CPE. The effects of some parameters, such as potential scan rate and concentration of carbohydrates are investigated. The rate constants for the catalytic reaction (k') of carbohydrates are also obtained. The size-selective electro-catalyst shows a good linear dependency on carbohydrates' concentration in the range of 0.01–0.06 M with the detection limit of 6.4 mM at the signal-to-noise ratio of 3. Furthermore, the modified electrode exhibits no interference with the simultaneous presence of stevioside. In brief, these results demonstrate that Ni^{II}{salnptn(4-OH)$_2$}-Y composites have a great potential for synthesizing size-selective electrocatalysts for determining the purity of stevioside.

© 2013 Elsevier B.V. All rights reserved.

1. Introduction

Providing a substitute for sucrose has attracted great attention due to the growing incidence of obesity and diabetes all over the world. Much attention has been focused on stevioside, a sweet glycoside extracted from Stevia rebaudiana Bertoni plant. Stevioside is an abundant component of Stevia rebaudiana leaf that has become well-known for its intense sweetness (250–300 times sweeter than sucrose) and is used as a non-caloric sweetener, both in the form of stevioside and stevia extract, in food and drug industry [1]. In 2006, the meeting of the Joint FAO/WHO Expert Committee on Food Additives (JECFA) to evaluate certain food additives and ingredients, flavoring agents, and natural constituents of food announced a temporarily accepted daily intake (ADI) of stevioside up to 5.0 mg/kg body weight (BW) [2].

At present, the incidence of some metabolic syndromes, such as type II diabetes mellitus and obesity are major public health concerns in industrialized and developing countries due to aging, dietary habits and a decrease in physical activities. Postprandial hyperglycemia observed in type II diabetes is usually due to an increase in basal hepatic glucose production and a decrease in peripheral glucose disposal. Therefore, there is a popular use of herbal and alternative medicine for the treatment of diabetes. In this regard, stevioside can be a good alternative to sugar for diabetic patients [3]. Early studies show that there is a significant decrease in blood glucose level following the use of certain amounts of stevioside [4,5]. These observations support the earlier notion that stevioside and stevia extract can be used to treat diabetic conditions. Because the simultaneous presence of some carbohydrates, such as glucose, sucrose and fructose with stevioside can be harmful to diabetics, it is necessary to detect these carbohydrates as impurities. A promising strategy consists of the use of inorganic microporous solids to host an electro-active guest to increase the selectivity and sensitivity of the modified electrode. Zeolite materials are identified at an early stage as promising candidates for the modification of electrodes due to their well-characterized crystalline structures having sub-nanometer diameter pores. A large number of publications in the past two decades have been devoted to the study of zeolite-modified electrodes (ZMEs), which frequently consist of a zeolite-polymer composite or a zeolite-impregnated carbon paste attached to an underlying conductor [6–10]. Studies on ZMEs mainly focus on the preparation methods of the modified electrode, electrochemical characterization of ion exchange and the electrode process as well as on the discussion of electron-transfer mechanism [11,12]. Only a few articles have dealt with the electroanalytical

* Corresponding author. Tel.: +98 21 22853551; fax: +98 21 22853650.
E-mail address: mjafarian@kntu.ac.ir (M. Jafarian).

0039-9140/$ - see front matter © 2013 Elsevier B.V. All rights reserved.
http://dx.doi.org/10.1016/j.talanta.2013.02.055

applications of ZMEs [13,14]. Immobilization of suitable molecular species in zeolitic cavities to prepare a new type of functional materials has attracted much attention in recent times [15–19]. In this regard, there have been many reports on the preparation and identification of zeolite-encapsulated transition metal complexes of Schiff-base ligands [20–23]. This material optimistically combines the advantages of homogeneous and heterogeneous catalytic systems and increases the lifetime of the catalyst by encapsulation as the degradation pathways, such as dimerization can be prevented. Given these characteristics, zeolite-encaged metal complexes are similar to enzymes where the catalytic center might be a transition metal ion and the protein provides stability and stearic constraints [24].

In line with our previous report, in which the encapsulation of Ni^{II}-(N,N′-bis(2,4-dihydroxyacetophenone)-2,2-dimethylpropandiimine into the cavities of Y zeolite was carried out for the first time, the modified carbon paste electrode (CPE) is prepared by incorporating the encapsulated complex in the carbon paste matrix (denoted as Ni^{II}{salnptn(4-OH)$_2$}/CPE) [25]. The molecular size of the supercage of zeolite Y in which the nickel Schiff-base complex is incorporated blocks the electrochemical oxidation of stevioside, enabling the determination of millimolar concentrations of glucose, fructose and sucrose in the presence of a large excess of stevioside in alkaline solutions. This modified electrode exhibits a potent and stable electro-catalytic activity toward the oxidation of carbohydrates. Moreover, the rate constants for the catalytic reactions of these carbohydrates are obtained.

2. Experimental

2.1. Materials and physical measurements

Stevioside hydrate ($C_{38}H_{60}O_{18}\times H_2O$; M_r=804.87; from *Stevia* sp.; ≥98%) is obtained from Isfahan Science and Technology Town (ISTT) and used as received. NaY zeolites are purchased from SPAG, Iran. The chemicals used in the synthesis of nickel Schiff-base complex and other reagents and solvents used are of analytical reagent grade Merck product and used as received without further purification. All aqueous solutions for electrochemical experiments are prepared by distilled water. The supporting electrolyte used throughout all experiments is a 1 M NaOH solution.

Electrochemical studies are carried out in a conventional three-electrode cell powered by an electrochemical system comprising of EG&G model 273A potentiostat/galvanostat. A PC through M270 commercial software runs the system via a GPIB interface. A coiled platinum wire serves as an auxiliary electrode and the potentials are measured against an Ag/AgCl/KCl (saturated) electrode. All measurements are carried out at 298 ± 2 K.

^{1}HNMR spectrum of the H_2{salnptn(4-OH)$_2$} Schiff-base ligand is obtained in DMSO solution on a Bruker FT-NMR 250 (250 MHz) spectrophotometer. The infrared spectra are recorded on a Unicam Matson 1000 FT-IR spectrometer. The spectra of the neat nickel Schiff-base complex and the zeolite-encapsulated complex are recorded as KBr pellets by mixing the samples well with KBr in 1:100 ratios. Elemental analyses (C, H, N) are performed using a Heraeus elemental analyzer CHN-O-Rapid (Elemental-Analyze system KBr pellets, West Germany). Powder X-ray diffraction (XRD) patterns are recorded on a Philips PW1800 powder X-ray diffractometer using Cu K_α radiation (λ=0.154178 nm). The SEM analyses are performed by VEGAII TESCAN electron microscope (Czech Republic) operating at an accelerating voltage of 15 kV. The samples are deposited on a brass holder and sputtered with gold. The chemical compositions of the samples are evaluated by scanning electron microscopy (SEM, SAMX) equipped with the energy dispersive X-ray (EDX).

2.2. Preparation of Ni^{II}{salnptn(4-OH)$_2$}-Y

The synthesis of the H_2{salnptn(4-OH)$_2$} Schiff-base ligand and its corresponding nickel Schiff-base complex are carried out according to the literature [26]. The encapsulation of the complex in zeolite Y is undertaken via the flexible ligand method, as described in electronic supplementary information.

2.3. Preparation of the working electrodes

In order to prepare the Ni^{II}{salnptn(4-OH)$_2$}-Y/CPE, 25 mg of Ni^{II}{salnptn(4-OH)$_2$}-Y is lightly ground together with 75 mg of graphite powder for about 15 min. This product is blended by mineral oil by a mortar and pestle to prepare the carbon paste. The resulting paste is tightly packed into one end of a glass tube (exposing geometric area of 0.064 cm^2), and a copper wire is introduced into the other end for electrical contact. A fresh electrode surface is generated rapidly by extruding a small plug of the paste with a stainless-steel rod and smoothing the surface on white paper until a smooth surface is observed. The cyclic voltammogram of the free complex is recorded in solution mode using 2×10^{-3} M solution of the Ni^{II}{salnptn(4-OH)$_2$} complex in a 1 M NaOH solution, on a CPE, and an electrode containing physical mixture of carbon paste and NaY zeolite, separately.

2.4. Computational details

All calculations have been performed at the density functional level (DFT) with the Gaussian09 program package [27]. We performed all electronic calculations in the gas phase without

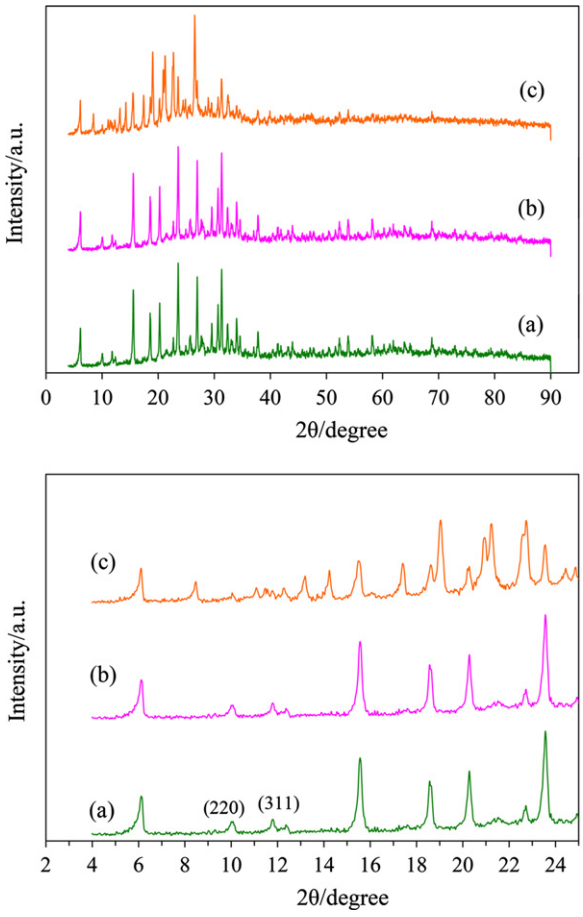

Fig. 1. (Top) XRD pattern of (a) NaY, (b) Ni-Y and (c) Ni^{II}{salnptn(4-OH)$_2$}-Y (bottom) expanded XRD patterns of a–c.

any symmetry constraints using the nonlocal hybrid density functional B3LYP [28,29], combining Becke's three-parameter hybrid exchange functional with the correlation functional of Lee et al. [30].

3. Results and discussion

3.1. X-ray powder diffraction studies

The basic question which is raised during any zeolite modification relates to the preservation of the original crystalline structure of zeolite. Comparative X-ray diffractometry (XRD) before and after the modification provides an answer to this question.

The powder X-ray diffraction patterns of the zeolite NaY, Ni-exchanged zeolites, and the encapsulated Ni^{II}{salnptn(4-OH)$_2$} complex in Ni-exchanged zeolites are shown in Fig. 1. Essentially similar diffraction patterns are witnessed in the encapsulated Ni^{II}{salnptn(4-OH)$_2$} Schiff-base and NaY, except that zeolite with encapsulated Ni^{II}{salnptn(4-OH)$_2$} Schiff-base shows diffraction lines having slightly weaker intensities. These observations indicate that the framework of the zeolite does not suffer any significant structural changes upon encapsulation. However, there are differences in the relative peak intensities of the (220) and (311) reflections appearing at $2\theta = 10^\circ$ and 12°, respectively. For pure zeolite-Y and for Ni-exchanged zeolite-Y, $I_{(220)} > I_{(311)}$, but for the encapsulated complex, $I_{(311)} > I_{(220)}$. This reversal in intensities has been empirically correlated with the presence of a large complex within the zeolite-Y supercage [31]. This change in

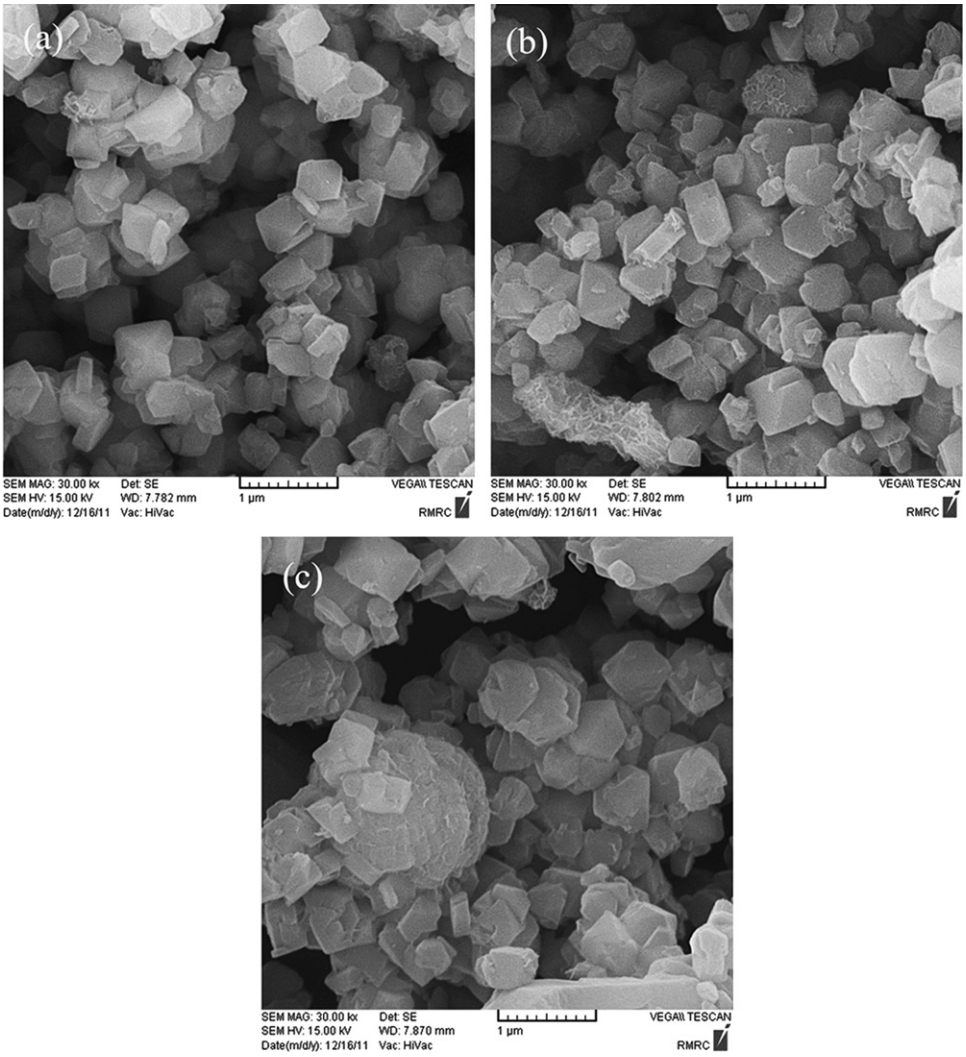

Fig. 2. SEM microphotographs of (a) NaY, (b) Ni-Y and (c) Ni^{II}{salnptn(4-OH)$_2$}-Y.

Table 1
Chemical composition analyses for NaY, Ni-Y, Ni^{II}{salnptn(4-OH)$_2$} and Ni^{II}{salnptn(4-OH)$_2$}-Y composite (the calculated values are represented in parenthesis).

Sample	Ni%	Si%	Al%	C%	N%	Si/Al ratio	C/N ratio
NaY	—	22.85	9.42	—	—	2.43	—
Ni-Y	5.55	21.03	8.84			2.38	—
NiII{salnptn(4-OH)2}	13.85 (13.74)	—	—	58.96 (59.053)	6.72 (6.56)	—	8.77 (9.01)
NiII{salnptn(4-OH)2}-Y	2.22	21.72	9.08	9.45	1.06	2.39	8.91

the relative intensities may be associated with the redistribution of randomly coordinated free cations in zeolite Y at sites II and I. The above observation may therefore be construed as evidence of the successful encapsulation of Ni^{II}\{salnptn(4-$OH)_2$\} complex within the supercage of zeolite Y.

3.2. Scanning electron microscopy (SEM) and chemical composition analysis

The SEM micrographs in Fig. 2 show that the original zeolite crystalline structure is preserved after the encapsulation of nickel Schiff-base complex. Furthermore, in the SEM taken after purification, no surface complexes are seen and the particle boundaries on the external surface of zeolite are clearly distinguishable, but zeolite crystalline structure of the Ni^{II}\{salnptn(4-$OH)_2$\}-Y sample seems to be degraded at the edges.

The results of chemical composition analysis obtained by EDX method are given in weight percents in Table 1. The Si/Al ratio of 2.4 corresponds to a unit cell formula $Na_{56}(AlO_2)_{56}(SiO_2)_{136}$ for parent NaY. The Si/Al ratio has remained unchanged in Ni-exchanged zeolites, indicating the absence of dealumination during the exchange process. The amounts of nickel content in the intrazeolite complexes are found to be lower compared to the Ni-exchanged zeolites. The decrease in the nickel content during complex formation inside the zeolite cavity can be attributed to the participation of nickel ion in the formation of coordination complexes inside the cavities of zeolite Y, or it may so happen that some of the nickel ions leach out during complex formation. The chemical analyses of the sample reveal the presence of organic material with a C/N ratio roughly similar to that of the neat complex. The C and N contents indicate a ligand/metal molar ratio of around 1, indicating nickel to have 1:1 coordination.

3.3. Infrared spectroscopy (FTIR)

Infrared spectra of NaY, Ni-Y, Ni^{II}\{salnptn(4-$OH)_2$\} complex and Ni^{II}\{salnptn(4-$OH)_2$\}-Y have been recorded to verify the encapsulation of nickel Schiff-base complex into the zeolite matrix (Fig. 3). A strong and a broad band at the region 1000 cm^{-1} could be attributed to the asymmetric stretching vibrations of Al–O–Si chain of zeolite. The broad bands in the region 1650 and 3500 cm^{-1} are due to the lattice water molecules and surface hydroxyl groups, respectively. The symmetric stretching and bending characteristic bands of Al–O–Si framework of the NaY zeolite appear at 789 and 725 cm^{-1}, respectively [32]. These bands are not modified during exchange with Ni^{+2} or by supporting the nickel complex which further implies

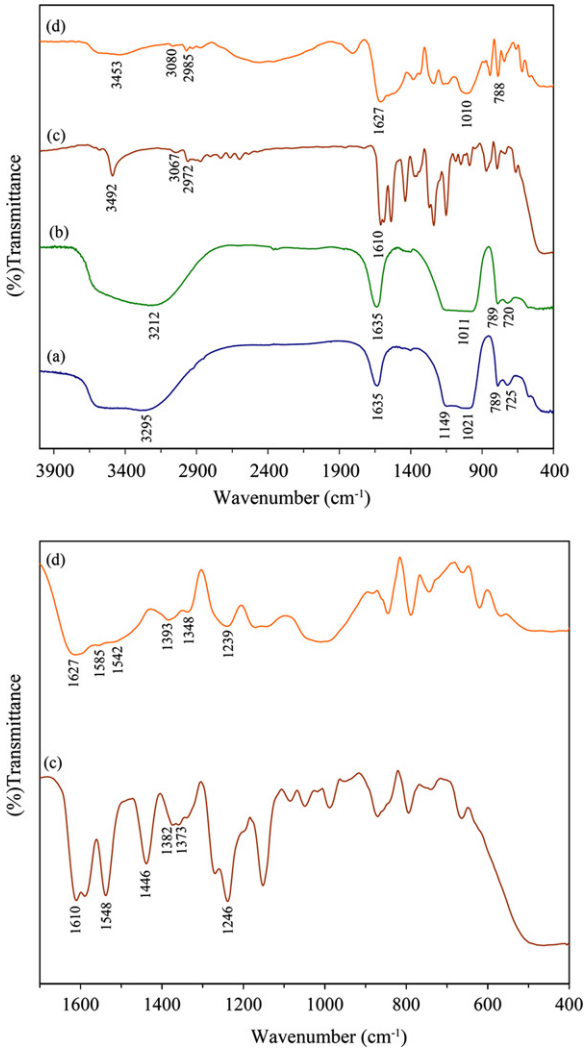

Fig. 3. (Top) FT-IR spectra of (a) pure zeoliteY, (b) Ni-Y, (c) Ni^{II}\{salnptn(4-$OH)_2$\} and (d) Ni^{II}\{salnptn(4-$OH)_2$\}-Y (bottom) expanded IR-spectrum of (c) and (d) in between 1700 and 400 cm^{-1}.

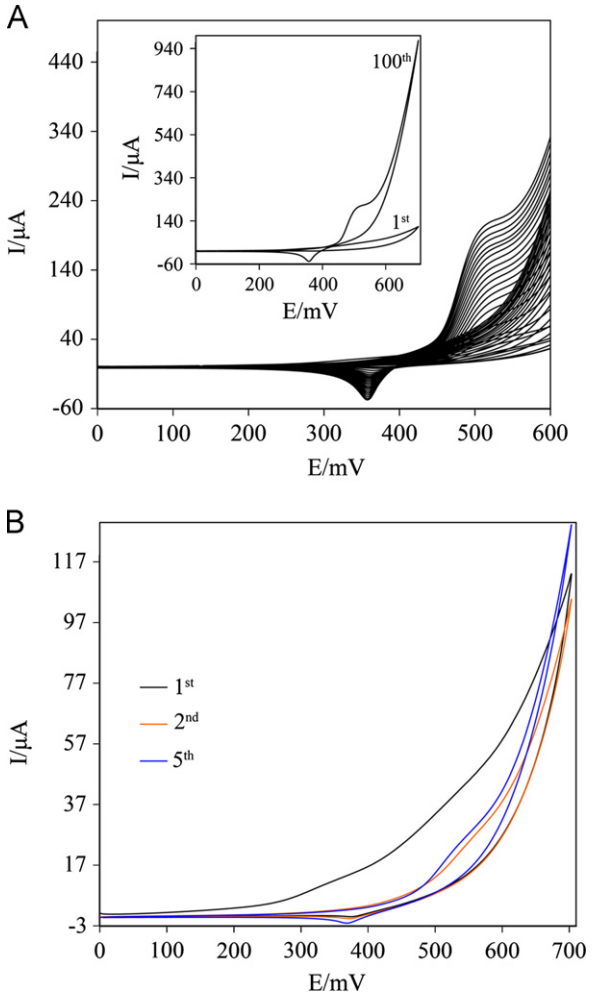

Fig. 4. (A) Consecutive cyclic voltammogram of Ni^{II}\{salnptn(4-$OH)_2$\}-Y/CPE oxidation in 1 M NaOH comprised of different sweep numbers (1, 2, 5, 10, 15, 20, 25, 30, 35, 40, 45, 50, 55, 60, 65, 70, 75, 80, 85, 90, 95, and 100) at a scan rate of 100 mV s^{-1}. Inset: the first and hundredth cyclic voltammogram. (B) The primary cyclic voltammograms of Ni^{II}\{salnptn(4-$OH)_2$\}-Y/CPE oxidation in 1 M NaOH.

that the zeolite framework has remained intact upon encapsulation of the nickel Schiff-base complex. The IR bands of the encapsulated complex are weak due to its low concentration in the zeolite cage and thus can only be observed in the region where the zeolite matrix does not show any absorption band that lies in the 1200–1600 cm^{-1} region. The FT-IR spectrum of the ligand shows two sharp bands appearing at 1548 and 1446 cm^{-1} which can be attributed to the azomethine group of Schiff-base ligands [33,34] (Provided in electronic supplementary information, Fig. S1C). The IR spectrum of the neat Ni^{II}{salnptn(4-$OH)_2$} complex (Fig. 3c) shows major bands at 1610 (C═C), 1548, 1446 (C═N), 1382, 1373 cm^{-1} ($\nu_{C(Me)_2}$ carbon backbone chain), and 1246 cm^{-1} (C–O). Similar frequencies are also observed in the case of the encapsulated complex in the NaY zeolite with a little shift in the C═N, C–O and $C(Me)_2$ bands to wavenumbers 1585, 1542 and 1240 cm^{-1}, respectively, indicating nitrogen and oxygen coordination inside the cavity of the zeolite framework. The $\nu_{C(Me)_2}$ bands at 1382 and 1373 cm^{-1} are shifted toward upper wavenumber, which indicates the encapsulation of the nickel Schiff-base complex inside the NaY zeolite.

3.4. Electrochemical studies

3.4.1. Electrochemistry of the Ni^{II}{salnptn(4-$OH)_2$}-Y Schiff-base complex

Cyclic voltammetry provides information on the nature of intrazeolite complexes that may not be readily revealed in spectroscopic studies. Zeolites are basically insulators, so the encapsulation of transition-metal complexes makes these molecular sieves to show redox behavior if they are encapsulated inside the cavities or bound to the surfaces within zeolite lattice. Fig. 4A represents consecutive cyclic voltammograms of Ni^{II}{salnptn(4-$OH)_2$}-Y/CPE in 1 M NaOH solution recorded at a scan rate of 100 mV s^{-1}. A pair of redox peaks appearing at 542 and 385 mV vs. Ag/AgCl in the early cycles is assigned to Ni^{II}/Ni^{III} redox reaction of the encapsulated nickel Schiff-base complex (Fig. 4B). The growth of current with the number of potential scans indicates the progressive enrichment of the accessible electroactive species in the nanocavities of zeolites [35–40] at the surface of the Ni^{II}{salnptn(4-$OH)_2$}-Y/CPE. The shift of peak

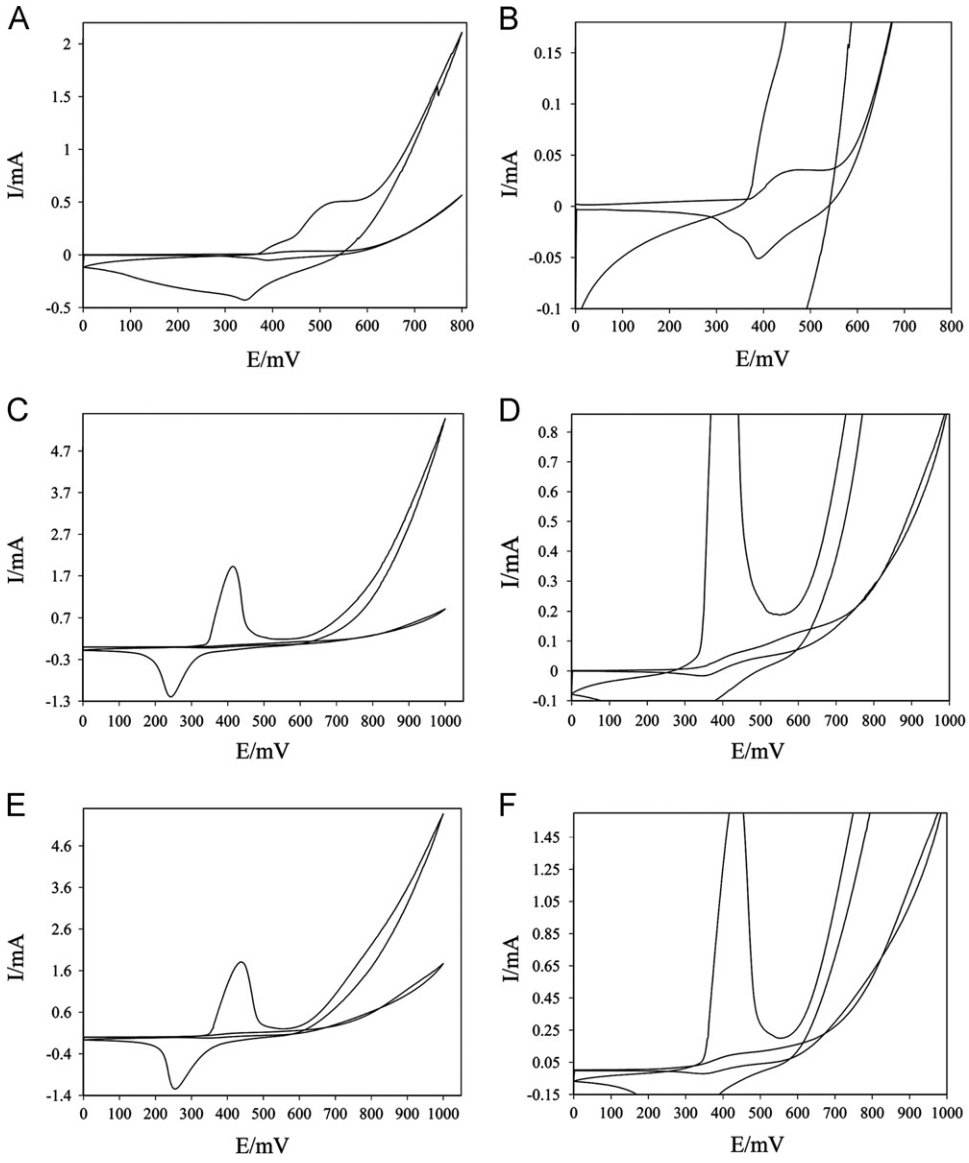

Fig. 5. Cyclic voltammogram of (a) NiY/CPE and (c) free Ni^{II}{salnptn(4-$OH)_2$} on the CPE and (e) free Ni^{II}{salnptn(4-OH)2} on the NaY+CPE (physical mixture) at a scan rate of 100 mV s^{-1}. (b, d, f) Expanded cyclic voltammograms of panels a, c, and e, respectively.

potentials indicates that the metal complex does not have the same geometry as that in the neat complex but does undergo distortion inside the zeolite matrix as reported previously [25].

To ascertain the redox peak observed at 542 and 385 mV vs. Ag/AgCl are assigned to Ni^{II}/Ni^{III} redox reaction, and also whether different electrochemical responses are due to uncomplexed Ni cations or nickel complexes present on the external surface, we recorded cyclic voltammograms for nickel exchanged NaY zeolite, carbon paste, and the physical mixture of carbon paste and NaY zeolites. The cyclic voltammogram characteristics and the peak potentials for nickel-exchanged NaY zeolite (Fig. 5a), carbon paste (Fig. 5c), and the physical mixture of carbon paste and NaY zeolites (Fig. 5e) (the Ni^{II}/Ni^{III} redox process) are entirely different from the encapsulated nickel Schiff-base complex. This indicates that $Ni^{II}\{salnptn(4\text{-}OH)_2\}$ complex is encapsulated inside the zeolite matrix and not present on the external surface. The peak broadening is observed after encapsulation of the metal complex in zeolite cage. This is because of the axial interaction of the metal complex with oxygen atoms at different locations in a zeolite. Charge distribution along the framework due to the partial ionic character of the aluminosilicate crystal generates a strong columbic field inside the cage of zeolites, which might activate the metal complex. Field gradients exist because of the zeolite geometry, cage, channels, side packets, and charge distribution [41].

The intrazeolite mechanism is proposed for electron transfer associated with encapsulated electroactive species entrapped in bulk zeolite. As these entrapped species cannot undergo any ion exchange reaction, the electron transfer occurs within the zeolite matrix via electron hopping processes [42]. Therefore, the electron transfer mechanism in accord with intrazeolite mechanism follows steps: (a) formation of $NiO\{salnptn(4\text{-}OH)_2\}$-Y in the presence of OH^- ions and (b) oxidation of metal as a consequence of the potential scanning to give rise to $Ni^{III}OOH\{salnptn(4\text{-}OH)_2\}$-Y

$$NiO\{salnptn(4-OH)_2\}-Y+OH^-+C_Z^+ \underset{k_{-1}}{\overset{k_1}{\rightleftarrows}} Ni^{III}OOH\{salnptn(4-OH)_2\}-Y+e+C_S^+ \quad (1)$$

where C^+ is an electrolyte cation and the subscripts z and s indicate zeolite and solution phases, respectively. After 100 cycles, the current practically reaches a steady state value and the redox peaks potentials are stabilized at 515 and 356 mV vs. Ag/AgCl (Fig. 4A). The current increase following the anodic wave is the result of the oxygen evolution reaction. The intensity of this reaction also slowly grows with advancing polarization, suggesting a correlation between the oxygen evolution and the concentration of Ni^{III} sites [43].

Because the negatively charged zeolite matrix is able to incorporate cationic species and repel anions, it combines size-exclusion and charge-exclusion properties. Therefore, once nickel Schiff-base complex is oxidized it becomes positively charge and strongly interacts with its zeolite cage. The coloumbic mismatch centered on Ni^{II}/Ni^{III} process and increase in peak currents with scan number is attributed to this interaction. In addition, the size of the $Ni^{II}\{salnptn(4\text{-}OH)_2\}$ complex (based on the reported computational results, 9–11 Å kinetic diameter) [25] is larger than the zeolite Y pore diameter (7.4 Å) and thus is not able to escape from the interior of the zeolite. At the concentration used in our experiments (1 M), anion penetration into the zeolite framework is significant and not influenced by electrostatic repulsion. As reported, the ingress of anions as ion pairs in aqueous media occurs only at solution concentrations above 1 M

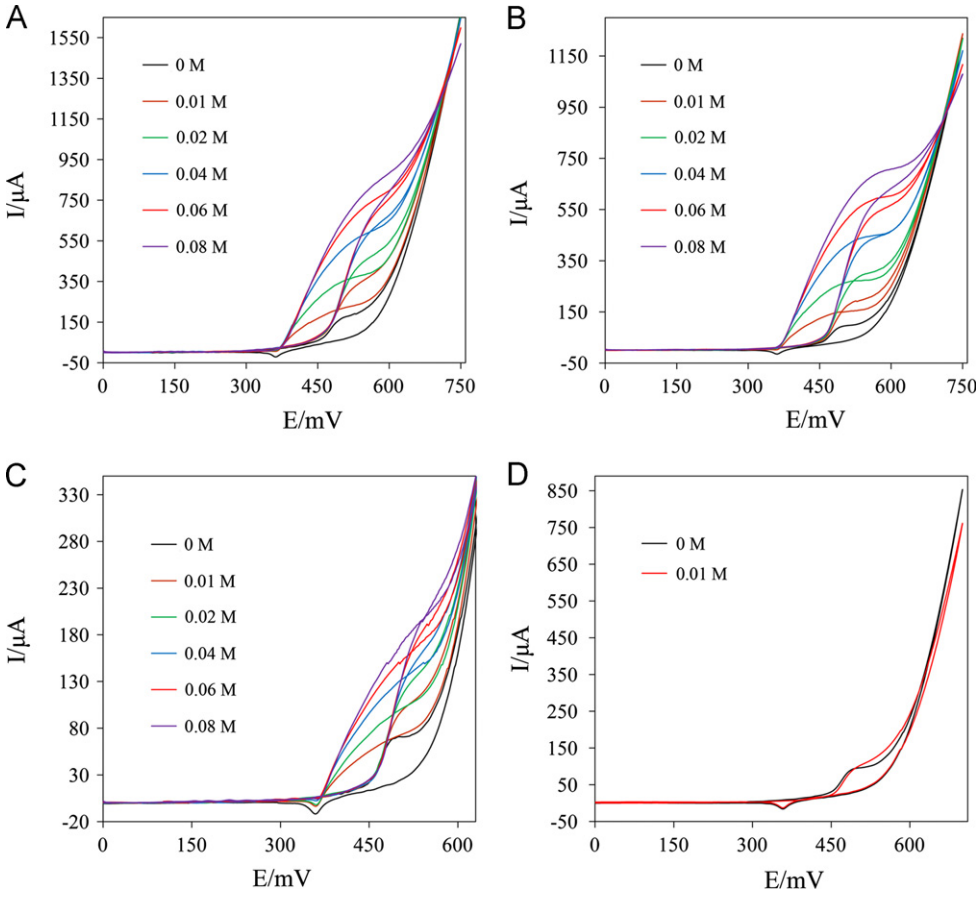

Fig. 6. Cyclic voltammograms of a $Ni^{II}\{salnptn(4\text{-}OH)_2\}$-Y/CPE in 1 M NaOH in the presence of different concentrations of (a) glucose, (b) fructose, (c) sucrose and (d) stevioside; scan rate 20 mV s^{-1}. (For interpretation of references to color in this figure, the reader is referred to the web version of this article.)

[44,45]. Therefore, our results with zeolite Y encapsulated nickel Schiff-base confirms that electron transfer to the complexes present within the zeolite channels proceeds via intrazeolite mechanism [46].

3.4.2. *Electrocatalytic oxidation of carbohydrates on Ni^{II}{salnptn(4-OH)$_2$}-Y/CPE*

This study shows that Ni^{II}{salnptn(4-OH)$_2$}-Y/CPE can act as a catalyst for electro-oxidation of some carbohydrates, such as glucose, fructose and sucrose. Fig. 6 A–C shows the cyclic voltammograms obtained when a Ni^{II}{salnptn(4-OH)$_2$}-Y/CPE is immersed in a solution containing different concentrations of the corresponding carbohydrates at a potential sweep rate of 20 mV s^{-1}. It is observed that the anodic current has increased on the modified surface in the presence of carbohydrates, and it is followed by a decrease in the cathodic current upon an increase in the concentration of carbohydrates in the solution. This result indicates that these carbohydrates are oxidized by an active nickel moiety through a cyclic mediation redox process [46]. Nickel species are immobilized in the nanocavities of zeolitic matrix, and the one with a higher valency oxidizes carbohydrates via a chemical reaction, followed by generating a low-valance nickel. Along this line, the high-valent nickel species are regenerated through the external electrical circuit. Accordingly, the carbohydrate oxidation process on Ni^{II}{salnptn(4-OH)$_2$}-Y catalysts should obey the mechanism proposed by Fleischmann and Pletcher [47], Fleischmann et al. [48] and Virtes and Horanyi [49] (see electronic supplementary information)

Fig. 6D shows the cyclic voltammograms measured for the Ni^{II}{salnptn(4-OH)$_2$}-Y catalysts in the presence of stevioside (the red line), in which the cyclic voltammogram in the absence of stevioside (the black line) is also shown for comparison. On Ni^{II}{salnptn(4-OH)$_2$}-Y/CPE, the oxidation process is significantly inhibited. This lack of response can be associated with the size-exclusion exerted by the zeolite framework with respect to the large size of stevioside molecules. To further amplify this conclusion, we precisely

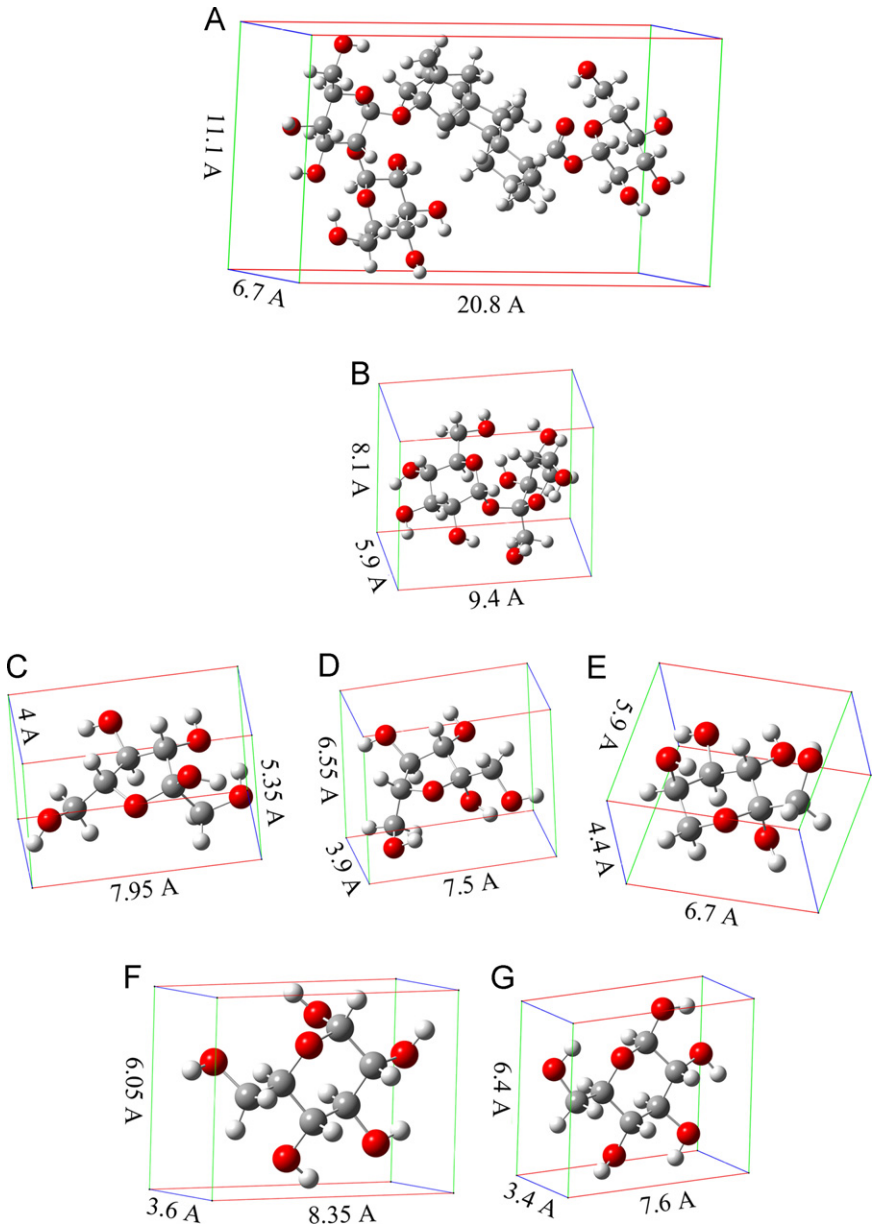

Fig. 7. The molecular structure and size of carbohydrate molecules: (a) stevioside (b) sucrose (c) α-D(-)-fructofuranose (d) β-D(-)-fructofuranose (e) D(-)-fructopyranose (f) α-D(+)-glucose (g) β-D(+)-glucose.

calculated the molecular sizes of the four investigated molecules. Based on optimized geometries, the three dimensional sizes of stevioside, glucose, fructose and sucrose are estimated to be $20.8 \times 6.7 \times 11.1$ Å^3, $7.6 \times 3.4 \times 6.4$ Å^3, $6.7 \times 5.9 \times 4.4$ Å^3 and $9.4 \times 5.9 \times 8.1$ Å^3 (see the dimensional sizes of other anomers of fructose and glucose in Fig. 7), respectively. Apparently, the first is largest (considering the solvation effect, the actual size of a moving stevioside molecule is larger than the theoretical molecular size obtained through the calculation). The pore size of zeolite Y is large enough to allow glucose, fructose and sucrose to pass through but inhibits the access of the larger molecule, stevioside, to the Ni^{II}{salnptn(4-OH)$_2$}-Y particles as presented in Scheme 1. The difference in molecular sizes led to significant distinction in electro-oxidation on Ni^{II}{salnptn(4-OH)$_2$}-Y/CPE.

The kinetic informations about the oxidation process of carbohydrates on the Ni^{II}{salnptn(4-OH)$_2$}-Y catalyst could be learnt through the evolution of CV curves at different potential scan rates (v) as shown in Fig. 8A. For further clarification, only the anodic half cycles are presented. Increasing the scan rate, in turn, resulted in an increase in the anodic peak current. A linear logarithmic dependence of anodic peak current on the scan rate is observed (Fig. 8B). It is found that the slope of this dependency is close to neither half or nor one as would be expected, respectively, for a purely diffusion or adsorptive response. Therefore, the nature of the electrodic process is analyzed by plotting $I_p/v^{1/2}$ as a function of $v^{1/2}$ as shown in Fig. 8C. The limiting value corresponds to the diffusion-controlled region, whilst the non-horizontal region corresponds to mixed controlled process (both diffusion and adsorption) in the 0.02 M glucose solution. Moreover, a plot of the scan rate-normalized current ($I_P/v^{1/2}$) with respect to the scan rate (Fig. 8C) exhibited the typical shape of an electrochemical–chemical (EC′) catalytic processes [50]. The same behavior is observed for fructose and sucrose.

The long-term stability of the catalyst is investigated under extensive cycling of Ni^{II}{salnptn(4-OH)$_2$}-Y/CPE in 1 M NaOH in the presence of 0.02 M glucose at a scan rate of 20 mV s^{-1} for 200 cycles (Fig. 9). It is observed that the current density of electro-oxidation of glucose is almost constant in 200 cycles indicating the stability of this electro-catalyst as well as no surface poisoning.

3.4.3. Chronoamperometric studies

Chronoamperometry is further employed to investigate the kinetics of the catalytic reaction. Fig. 10A shows the double-step chronoamperograms for Ni^{II}{salnptn(4-OH)$_2$}-Y/CPE in the absence (a) and the presence (b–f) of fructose over a concentration range

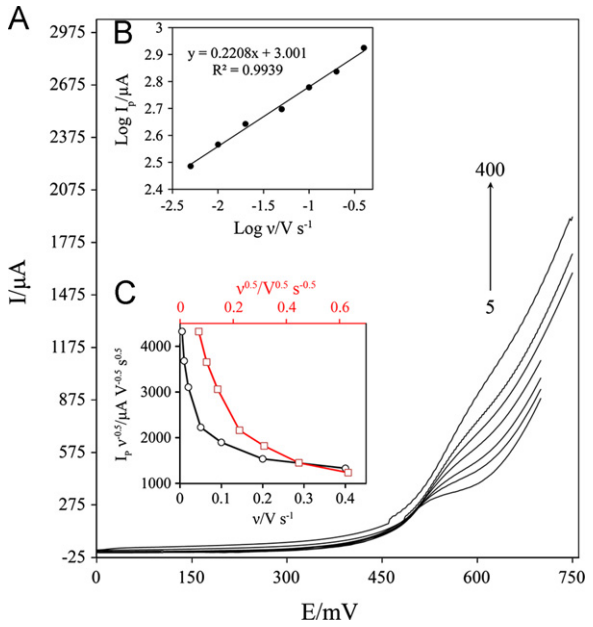

Fig. 8. (A) Typical cyclic voltammograms (only the anodic sweeps are presented) of the Ni^{II}{salnptn(4-OH)$_2$}-Y/CPE in 1 M NaOH in the presence of 0.02 M glucose at various potential sweep rates of 5, 10, 20, 50, 100, 200 and 400 mV s^{-1}. (B) Dependence of the logarithm of anodic peak current during the forward sweep on the logarithm of sweep rate. (C) The anodic current function ($I_{Pa}/v^{1/2}$) vs. potential sweep rate (v) and the square roots of sweep rate ($v^{1/2}$).

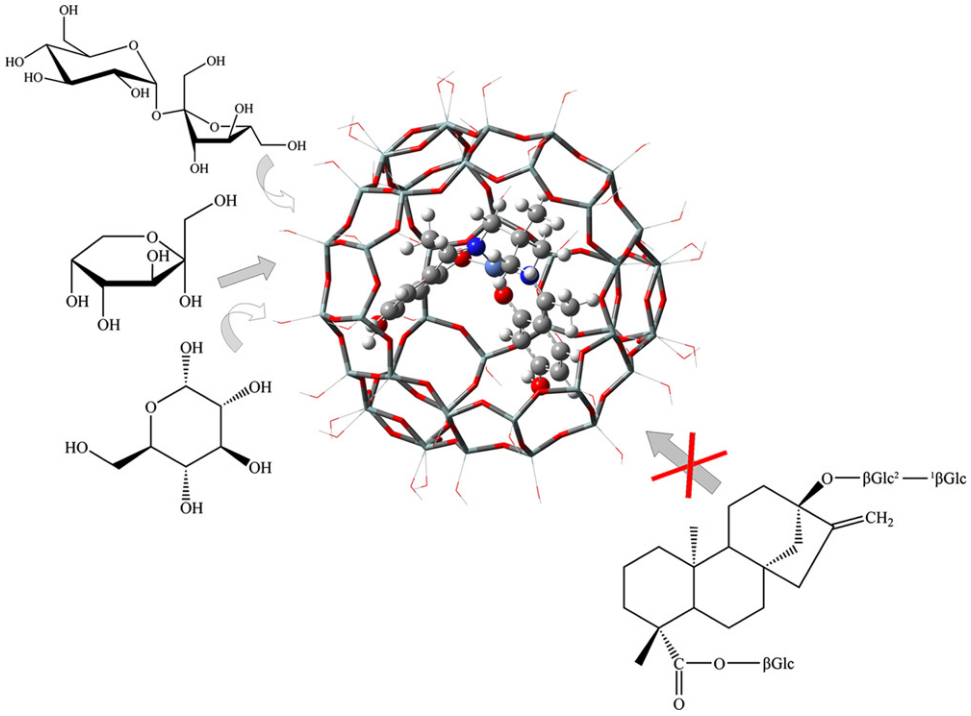

Scheme 1. Schematic the rationale of the size selectivity over Ni^{II}{salnptn(4-OH)$_2$}-Y.

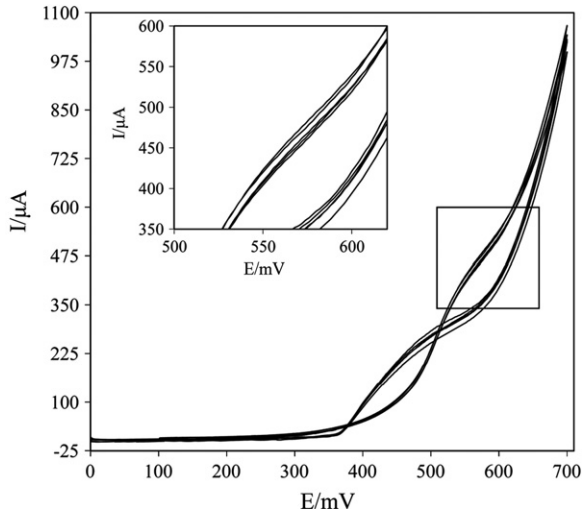

Fig. 9. Repeated cyclic voltammograms of 0.02 M glucose oxidation on N Ni^{II} {salnptn(4-$OH)_2$}-Y/CPE at 20 mV s^{-1}, cycle number 1, 50, 100, 150, 200.

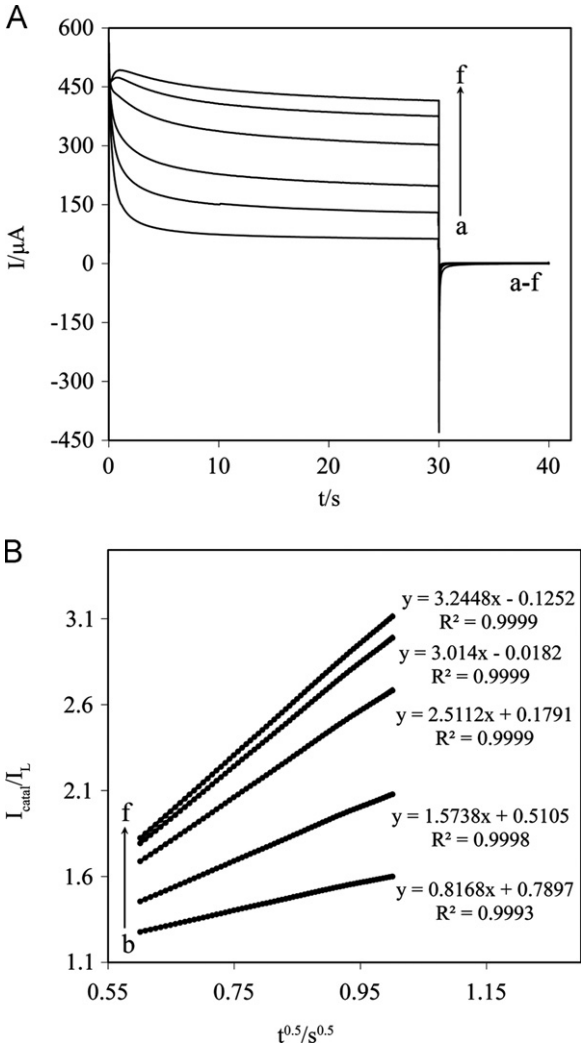

Fig. 10. (A) Double steps chronoamperograms of Ni^{II}{salnptn(4-$OH)_2$}-Y/CPE in 1 M NaOH solution containing glucose over a concentration range of 0.01–0.08 M. Potential steps were 530 mV for oxidation and 0 mV for reduction. (B) Dependence of I_{catal}/I_L on $t^{0.5}$ derived from the data of chronoamperograms in part A.

of 0.01–0.08 M. The applied potential steps are 530 and 0 mV vs. Ag/AgCl, respectively. The current is also negligible when the potential is stepped down to 0 mV, indicating the irreversibility of the fructose oxidation process.

Chronoamperometry is also be used to obtain the catalytic rate constant. According to [49]:

$$I_{catal}/I_L = \lambda^{0.5}[\pi^{0.5} erf(\lambda^{0.5}) + \exp(-\lambda)/\lambda^{0.5}] \quad (2)$$

where I_{catal} and I_L are the currents in the presence and the absence of fructose and $\lambda = k' C_s t$ is the argument of the error function. k' is the catalytic rate constant and t is the elapsed time. In the cases where $\lambda > 1.5$, erf($\lambda^{1/2}$) is almost equal to unity, so the above equation can be reduced to:

$$I_{catal}/I_L = \pi^{0.5}\lambda^{0.5} \quad (3)$$

From the slope of the I_{catal}/I_L vs. $t^{1/2}$ plot, presented for different concentrations of fructose in Fig. 10B, the mean value of k' for fructose has been obtained to be around 4.02×10^4 cm^3 mol^{-1} s^{-1}. Similar chronoamperograms have been obtained for glucose and sucrose, and the corresponding values of k' obtained according to the method described above for these carbohydrates are 2.8×10^4 and 1.00×10^4 cm^3 mol^{-1} s^{-1}, respectively. k' values also confirm that the Ni^{II}{salnptn(4-$OH)_2$}-Y/CPE approximately exhibits approximately similar catalytic activity toward the oxidation of the mentioned carbohydrates.

From these results, we can conclude that the electrode modified with zeolite-encapsulated nickel Schiff-base complex could be

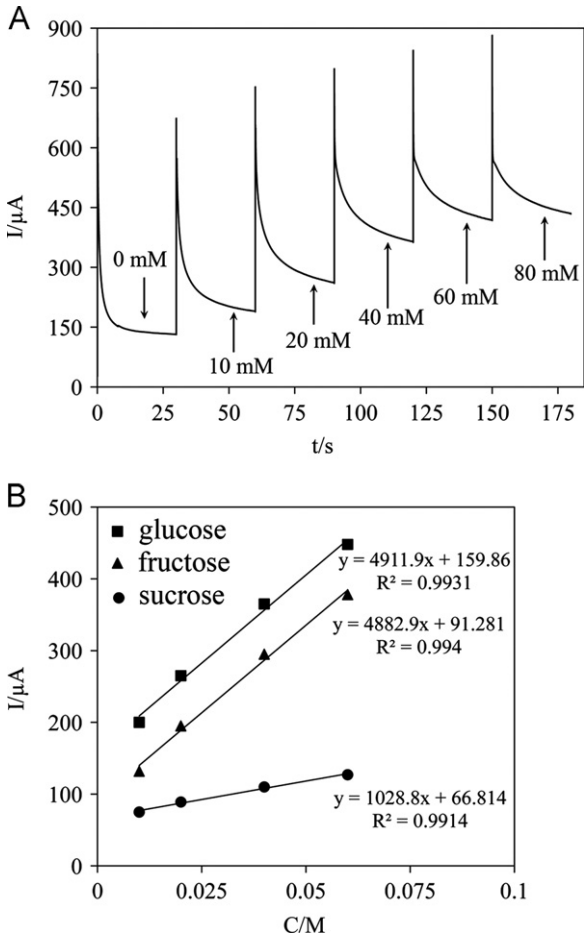

Fig. 11. (A) Amperometric response of the Ni^{II}{salnptn(4-$OH)_2$}-Y/CPE with successive additions of glucose to 1 M NaOH solution at an applied potential of 530 mV. (B) Calibration curves obtained from chronoamperometric measurments for glucose, fructose and sucrose.

Table 2
Analytical parameters calculated from the calibration curve for electrocatalytic oxidation of glucose, fructose and sucrose obtained from amperometry.

Carbohydrates	LOD (*M*)	LOQ (*M*)	Linear range (*M*)
Glucose	6.8×10^{-3}	2.3×10^{-2}	0.01–0.06
Fructose	6.4×10^{-3}	2.1×10^{-2}	0.01–0.06
Sucrose	7.6×10^{-3}	2.5×10^{-2}	0.01–0.06

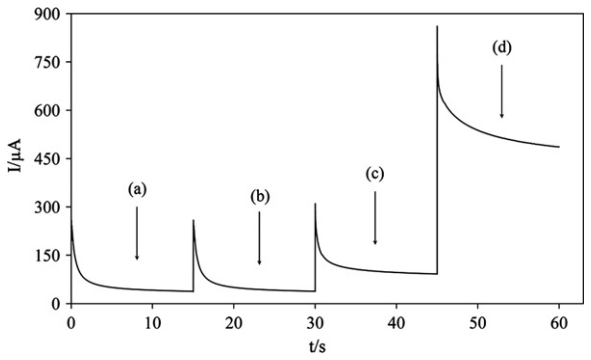

Fig. 12. Amperometric response of Ni^{II}{salnptn(4-OH)$_2$}-Y/CPE to (a) bare (b) 20 mM stevioside and different interferences of (c) 20 mM sucrose and (d) 60 mM fructose in stirring 1 M NaOH solution. The working potential was 530 mV.

used for determining small molecular size carbohydrates in the presence of stevioside.

In order to evaluate the performance of the Ni^{II}{salnptn(4-OH)$_2$}-Y/CPE as an amperometric sensor for glucose detection, hydrodynamic amperometry in a batch system is applied by poising the modified electrode at a potential of 530 mV. According to results (see Fig. 11A), the amperometric sensor response is moderately rapid, since it takes less than 10 s to obtain a steady-state current after the addition of glucose to 10 mL of a 1 M NaOH solution. Gentle stirring for a few seconds is needed to promote the homogenization of the solution after each injection. Fig. 11B depicts typical calibration curves obtained from chronoamperometric measurments for glucose, fructose and sucrose. The sensitivity is calculated from the slope of the linear part of the plot. The detection limit is calculated as the concentration that gives a signal which is equal to three times the standard deviation of the background. Similar chronoamperogram is obtained for fructose and sucrose. LODs and LOQs for determining these carbohydrates are summarized in Table 2. From these results, it can be concluded that the electrodes modified with nanocomposite of Ni^{II}{salnptn(4-OH)$_2$}-Y could be used as sensors for determining carbohydrates.

It is known that selectivity is a very important aspect of sensor performance. As shown in Fig. 12, it is found that the current response almost does not change after the addition of the 0.02 M concentration of stevioside. After successive additions of different analytes, a 20 mM sucrose and 60 mM fructose, respectively, which are injected into the solution, a current response equal to those at the first injection is caused, indicating the high selectivity of the Ni^{II}{salnptn(4-OH)$_2$}-Y/CPE.

4. Conclusion

In this research, nickel Schiff-base complexes are encapsulated in the nanopores of Na-Y zeolites using the flexible ligand method. There are clear electrochemical and spectrochemical evidences for confirming the well-defined inclusion and distribution of the complex inside the zeolite matrix. The results of the spectrochemical and electrochemical study support that the encapsulated complex undergoes distortion under the influence of a constrained zeolite framework. The Ni^{II}{salnptn(4-OH)$_2$}-Y/CPE exerts (i) a blocking effect on stevioside oxidation and (ii) a catalytic activity for the electrochemical oxidation of small molecular size carbohydrates, such as glucose, fructose and sucrose. Considering this point, the Ni^{II}{salnptn(4-OH)$_2$}-Y/CPE can be effectively used for the determination of low concentrations of mentioned carbohydrates in the presence of stevioside, using CV and CA methods. The oxidation of carbohydrates on the Ni^{II}{salnptn(4-OH)$_2$}-Y/CPE is catalyzed through the mediated electron transfer. The stevioside sensor prepared as such also has excellent properties, such as good sensitivity, low detection limit, wide linear range, good selectivity and stability, indicating that Ni^{II}{salnptn(4-OH)$_2$}-Y nanocomposites are promising electrocatalysts for amperometric detection of other small molecular size carbohydrates as impurities which co-exist with stevioside. The reported data constitute a further example of the new opportunities offered by zeolite-confined species to be used as electrochemical sensors. The possibility of incorporating different species into the zeolite channel system and modulating the electrochemical properties of the encapsulated species that have been modified by the zeolite framework (assisted by DFT calculations) may result in an increase in the sensitivity and selectivity of electrochemical sensors.

Acknowledgments

We are grateful to Dr. Sogand Noroozizadeh for her impressive comments on the linguistic accuracy of this report. In addition, we would like to express our gratitude to Isfahan Science and Technology Town (ISTT), in particular Mr. Farshid Hendi, for providing stevioside samples for us. Iranian Nano Technology Initiative Council is gratefully acknowledged for financial support of this work.

Appendix A. Supporting information

Supplementary data associated with this article can be found in the online version at http://dx.doi.org/10.1016/j.talanta.2013.02.055.

References

[1] V. Chatsudthipong, Ch. Muanprasat, Pharmacol. Ther. 121 (2009) 41–54.
[2] JECFA, Joint FAO/WHO Expert Committee on Food Additives. Steviol glycosides [Addendum to stevioside]. In: Safety Evaluation of Certain Food Additives: Sixty third Meeting of the Joint FAO/WHO Expert on Food Additives, June 8–17, Geneva, 2005. Food and Agriculture Organization of the United Nations (FAO)/World Health Organization (WHO), Geneva, WHO Food Additives Series, No. 54, 2006, pp. 117–144 and 638.
[3] A.D. Kinghorn, D.D. Soejarto, Pure Appl. Chem. 74 (2002) 1169–1179.
[4] H. Susuki, T. Kasai, M. Sumihara, Nippon Nogei Kagaku Kaishi 51 (1977) 171–173.
[5] R. Curi, M. Alvarez, R.B. Bazotte, L.M. Botion, J.L. Godoy, A. Bracht, Braz. J. Med. Biol. Res. 19 (1986) 771–774.
[6] C.G. Murray, R.J. Nowak, D.R. Rolison, J. Electroanal. Chem. 164 (1984) 205–210.
[7] B. De Vismes, F. Bedioui, J. Devynck, C. Bied-Charreton, J. Electroanal. Chem. 187 (1985) 197–202.
[8] M.D. Baker, M. McBrien, I. Burgess, J. Phys. Chem. B 102 (1998) 2905–2907.
[9] V. Ganesan, R. Ramaraj, Langmuir 14 (1998) 2497–2501.
[10] C.B. Ahlers, J.B. Talbot, Electrochim. Acta 45 (2000) 3379–3387.
[11] C.A. Bessel, D.R. Rolison, J. Phys. Chem. B 101 (1997) 1148–1157.
[12] F. Bedioui, J. Devynck, J. Phys. Chem. 100 (1996) 8607–8609.
[13] M.D. Baker, C. Senaratne, Anal. Chem. 64 (1992) 697–700.
[14] B. Chen, N.K. Goh, L.S. Chia, Electrochim. Acta 42 (1997) 595–604.
[15] M. Sykora, J.R. Kincaid, Nature 387 (1997) 162–164.

[16] I.F.J. Vankelecom, D. Tas, R.F. Parton, V. Van de Vyver, P.A. Jacobs, Angew. Chem. Int. Ed. Engl. 35 (1996) 1346–1348.
[17] J.A. Incavo, P.K. Dutta, J. Phys. Chem. 94 (1990) 3075–3081.
[18] M. Sykora, K. Maruszewski, S.M. Treffert-Ziemelis, J.R. Kincaid, J. Am. Chem. Soc. 120 (1998) 3490–3498.
[19] F. Bedioui, Coord. Chem. Rev. 144 (1995) 39–68.
[20] C. Jin, W. Fan, Y. Jia, B. Fan, J. Ma, R. Li, J. Mol. Catal. A Chem. 249 (2006) 23–30.
[21] P.K. Saha, B. Dutta, S. Jana, R. Bera, S. Saha, K. Okamoto, S. Koner, Polyhedron 26 (2007) 563–571.
[22] J. Połtowicz, K. Pamin, E. Tabor, J. Haber, A. Adamski, Z. Sojka, Appl. Catal. A 299 (2006) 235–242.
[23] M. Silva, C. Freire, B. De Castro, J.L. Figueiredo, J. Mol. Catal. A Chem. 258 (2006) 327–333.
[24] S. Deshpande, D. Srinivas, P. Ratnasamy, J. Catal. 188 (1999) 261–269.
[25] M. Jafarian, M. Rashvand avei, M. Khakali, F. Gobal, S. Rayati, M.G. Mahjani, J. Phys. Chem. C 116 (2012) 18518–18532.
[26] S.A. Fairhurst, D.L. Hughes, U. Kleinkes, G.J. Leigh, J.R. Sanders, J. Weisner, J. Chem. Soc. Dalton Trans. 1995 (1995) 321–326.
[27] M.J. Frisch, et al., Gaussian 09, Revision A.1, Gaussian, Inc., Wallingford, CT, 2009.
[28] J. Weber, H. Huber, H.P. Weber, Chimia 47 (1993) 57–59.
[29] P. Geerlings, F.D. Proft, W. Langenaeker, Chem. Rev. 103 (2003) 1793–1873.
[30] C. Lee, W. Yang, R.G. Parr, Phys. Rev. B 37 (1988) 785–789.
[31] W.H. Quayle, J.H. Lunsford, Inorg. Chem. 21 (1982) 97–103.
[32] R.M. Barrer, Hydrothermal Chemistry of Zeolite, Academic Press, New York, 1982.
[33] R.M. Silverstein, G.C. Bassler, Spectrometric Identification of Organic Compounds, John Wiley & Sons, Inc., New York, 1963.
[34] P.K. Saha, S. Koner, Inorg. Chem. Commun. 7 (2004) 1164–1166.
[35] M. Jafarian, M. Rashvand avei, F. Gobal, S. Rayati, M.G. Mahjani, Electrocatalysis 2 (2011) 163–171.
[36] A.A. El-Shafei, J. Electroanal. Chem. 471 (1999) 89–95.
[37] G.W.D. Briggs, P.R. Snodin, Electrochim. Acta 27 (1982) 565–572.
[38] F. Hahn, B. Beden, M.G. Croissant, C. Lamy, Electrochim. Acta 31 (1986) 335–342.
[39] J. Desilvestro, D.A. Corrigan, M.J. Weaver, J. Electrochem. Soc. 135 (1988) 885–892.
[40] R. Barnard, C.F. Randell, J. Appl. Electrochem. 13 (1983) 89–95.
[41] G.O.A. Janssens, B.G. Baekelandt, H. Toufar, W.J. Mortier, R.A. Schoonheydt, J. Phys. Chem. 99 (1995) 3251–3258.
[42] Z. li, C. Lai, T.E. Mallouk, Inorg. Chem. 28 (1989) 178–182.
[43] B.E. Conway, T.C. Liu, J. Chem. Soc. Faraday Trans. 83 (1987) 1063–1080.
[44] C. Senaratne, J. Zhang, M.D. Baker, C.A. Bessel, D.R. Rolison, J. Phys. Chem. 100 (1996) 5849–5862.
[45] B.R. Shaw, K. Creasy, C.L. Lanczycki, J. Sargeant, M. Tirhado, J. Electrochem. Soc. 135 (1988) 869–876.
[46] I. Danaee, M. Jafariana, F. Forouzandeh, F. Gobal, M.G. Mahjani, Int. J. Hydrogen Energy 33 (2008) 4367–4376.
[47] M. Fleischmann, D. Pletcher, J. Electroanal. Chem. 31 (1971) 39–49.
[48] M. Fleischmann, K. Korinek, D. Pletcher, J. Chem. Soc. Perkin Trans. 10 (1972) 1396–1403.
[49] G. Virtes, G. Horanyi, J. Electroanal. Chem. 52 (1974) 47–53.
[50] R.S. Nicholson, I. Shain, Anal. Chem. 36 (1964) 706–723.